Numerical Investigation of Multiple Scattering and Mode-Converted Shear Waves Caused by Temporal Bone in Transcranial Photoacoustic Imaging

Hosseini, Fatemeh; Mozaffarzadeh, Moein; Mahlooiifar, Ali; Verweij, Martin D.; De Jong, Nico

DOI
10.1109/IUS54386.2022.9957367

Publication date
2022

Document Version
Final published version

Published in
IUS 2022 - IEEE International Ultrasonics Symposium

Citation (APA)
Hosseini, F., Mozaffarzadeh, M., Mahlooiifar, A., Verweij, M. D., & De Jong, N. (2022). Numerical Investigation of Multiple Scattering and Mode-Converted Shear Waves Caused by Temporal Bone in Transcranial Photoacoustic Imaging. In *IUS 2022 - IEEE International Ultrasonics Symposium* (IEEE International Ultrasonics Symposium, IUS; Vol. 2022-October). IEEE. https://doi.org/10.1109/IUS54386.2022.9957367

Numerical Investigation of Multiple Scattering and Mode-Converted Shear Waves Caused by Temporal Bone in Transcranial Photoacoustic Imaging

Fatemeh Hosseini
Departement of Computer and Electrical Engineering
Tarbiat Modares University
Tehran, Iran
fatemehsadathoseini@modares.ac.ir

Moein Mozaffarzadeh
Department of Imaging Physics
Technical University of Delft
Delft, The Netherlands
m.mozaffarzadeh@tudelft.nl

Ali Mahloojifar
Departement of Computer and Electrical Engineering
Tarbiat Modares University
Tehran, Iran
mahlooji@modares.ac.ir

Martin D. Verweij
Department of Imaging Physics
Technical University of Delft
Delft, The Netherlands
M.D.Verweij@tudelft.nl

Nico de Jong
Department of Imaging Physics
Technical University of Delft
Delft, The Netherlands
Nicolaas.deJong@tudelft.nl

2022 IEEE International Ultrasonics Symposium (IUS) | 978-1-6654-6657-8/22/$31.00 ©2022 IEEE | DOI: 10.1109/IUS54386.2022.9957367

Abstract— **In recent years, transcranial photoacoustic (TPA) imaging has become a popular modality for diagnosis of brain disorders. However, due to the presence of skull, TPA images are strongly degraded. Acoustically, this degradation is mainly categorized into the phase aberration, mode-converted shear waves, and multiple scattering. Previous studies numerically investigated the effects of mode-converted shear waves and multiple scattering on TPA images while the phase aberration caused by the skull was ignored and a conventional delay-and-sum method was employed for reconstructing TPA images. In this paper, we investigate these effects while a refraction-corrected image reconstruction approach is used to form TPA images. This approach enables separating the effects of phase aberration, mode-converted shear wave and multiple scattering. A realistic human temporal bone based on a MicroCT was used in the numerical model. In average for all the absorbers, the power of the artifacts caused by the mode-converted shear wave and multiple scattering are -13.7 dB and -20.1 dB when the refraction is corrected during image formation, respectively. These values were -7.9 and -18.8 if the conventional reconstruction is used. Accounting for phase aberration enables accurate quantification of the effects of the mode-converted shear waves and multiple scattering, which is necessary for evaluating the methods developed for degrading these effects.**

Keywords—Transcranial photoacoustic imaging, Temporal bone, Phase aberration correction, Multiple scattering, Mode-converted shear waves.

I. INTRODUCTION

Photoacoustic imaging (PAI) is a hybrid modality which provides the contrast of the optical imaging and resolution of the ultrasound imaging. By irradiation of a short electromagnetic pulse into the medium, local temperature rises and results in an initial pressure distribution. Via thermoelastic expansion effect, the pressure distribution then propagates through the medium and are detected by ultrasound transducers. An image representing the map of initial pressure distribution (proportional to the absorbed optical distribution energy) can be then reconstructed by processing the recorded A-lines [1,2].

Recent studies show the advantages of transcranial PAI (TPAI) for diagnosis of brain disorders like strokes [3] and hypoxic-ischemic encephalopathy [4]. There are several modalities that are currently used for brain imaging which include x-ray computed tomography (CT), magnetic resonance imaging (MRI), and position emission tomography (PET). Despite of their advancements, they are non-portable and relatively expensive. Moreover, CT and PET use ionizing radiations [5–7]. TPAI is a nonionizing and relatively low-cost with a spatial resolution determined by the acoustical properties of the transducer [8]. The presence of skull makes the medium acoustically heterogeneous though. Consequently, photoacoustic (PA) waves face with absorption inside the bone layer and cause multiple scattering and mode-converted shear waves [9,10].

Previous studies conducted numerical investigations of mode-converted shear waves and multiple scattering on PA signals while the phase aberration caused by the skull was ignored (i.e., a conventional delay-and-sum method was used for forming the images) [10,11]. Consequently, 1) the effects of mode-converted shear waves were combined with the effects of phase aberration considering that the mode-converted shear-waves arrive slightly after the compressional wave used for image formation, 2) while the artifacts caused by the multiple scattering appear after the actual absorber, they look prominent in the TPA images because they appear relative to the mainlobe, and the energy of the mainlobe is degraded due to improperly back-projecting the detected waves to the pixels of the image.

Recently, we have developed an image reconstruction technique that corrects for the effect of phase aberration and shown its applicability for PAI through a cortical bone replica [12], in vivo ultrasound imaging of the inner structure of the radius and tibia bone [13] and transcranial ultrasound imaging through the temporal window of a real human skull [14–17].

In this paper, we numerically investigate the effects of mode-converted shear waves and multiple scattering while the phase aberration caused by the bone layer is corrected during image reconstruction by employing the accurate travel times. To calculate the accurate travel times between elements of the probe and pixels, the sound speed map (obtained either by ultrasound images [16,17] or CT scans

[18]) is given to an eikonal solver. For quantification, the power of the mode-converted shear waves and multiple scattering (after normalizing the image to the local maximum) are reported. Our reconstruction approach enables separation of the effects of the phase aberration from mode-converted shear waves and multiple scattering. We expect that our approach and results give better and a more comprehensive understanding of the effects of mode-converted shear wave and multiple scattering on the TPA images.

II. MATERIALS AND METHODS

A. *Simulations*

A three layers medium (soft tissue, temporal bone, soft tissue; (Fig. 1)) was defined in the SimSonic2D to simulate the propagation of PA waves. The SimSonic is an open-source software for the 2-D and 3-D simulations of ultrasonic waves propagation through a desired medium. It employs finite-difference time-domain to solve the elastodynamic wave equation which makes it possible to simulate wave propagation either in the fluid or the elastic mediums [19]. To account for the both effects of mode-converted shear waves and multiple scattering, the simulation was run in the elastic mode. The thickness map of a realistic temporal bone was segmented from a high-resolution microCT data with a pixel size of 21 µm [20]. The thickness map of the temporal bone was interpolated with a factor of 3 and the pixel size was assumed 5 µm in the SimSonic for simplicity. The bone thickness varies between 1.1 mm and 4.9 mm. The minimum distance of temporal window from the probe was 3 mm, to mimic the skin [21]. The axial and lateral size of the medium was 30 mm × 41 mm, respectively. Three PA sources were placed in the axial and lateral coordinates of -5, 0, 5 mm and 15, 20, 25 mm, respectively. The size of each PA source defined as one grid which is 5 µm. A linear array transducer with the properties of L7-4 (pitch= 0.298 mm, central frequency= 5.2 MHz, 128 elements) was positioned to assemble the RF-data. Due to the limitations of the SimSonic, both the compressional and shear absorptions of the temporal bone was set 1.4 dB/mm which is the absorption of compressional wave in the central frequency (5.2 MHz); in practice, the absorption of the shear waves in a bone layer is almost twice that of the compressional wave and both are frequency-dependent [22].

As it was difficult to distinguish the effects of model-converted shear waves and multiple scattering when a realistic bone model was used and for better clarification, we also modeled a 2.5 mm flat bone [23]. A broadband PA source were placed in lateral and axial coordinate of 0 mm and 20 mm, respectively. All the images were shown after envelope detection, normalization and log compression.

B. *Reconstruction technique*

Our reconstruction technique, consists of two main steps [14–17]:

1) an Eikonal solver was used to calculate the travel times between the image pixels and the elements of transducer array given a sound speed map,

2) an adaptive delay-and-sum was used to form the TPA image given the correct travel times.

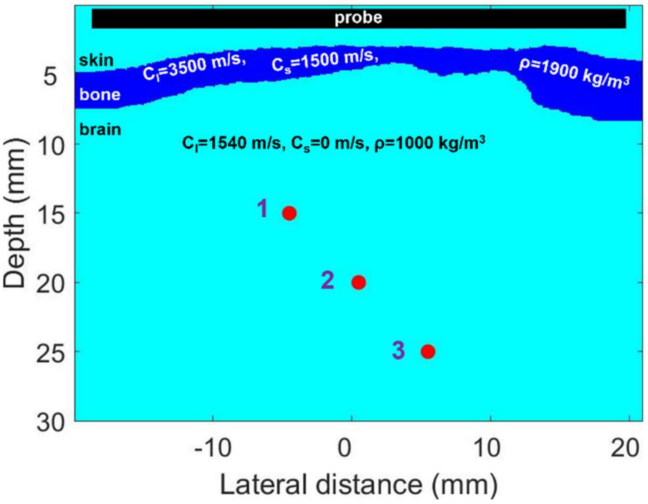

Fig. 1. The numerical model used in SimSonic. The temporal bone extracted from a microCT data [20]. 'C_l', 'C_s', and 'ρ' indicate the compressional wave speed, shear wave speed, and density of each layer, respectively. The black rectangle and the red circles show the position of the transducer array and the photoacoustic (PA) sources, respectively. The numbers are used to refer to the PA absorbers.

C. *Evaluation metrics*

To evaluate the improvements of our reconstruction method, the full-width-half-maximum (FWHM) and absorber-to-clutter ratio (ACR) were used. FWHM is defined as the width of the mainlobe at -6 dB. The ACR is defined as follows,

$$\mathrm{ACR} = 20 \times \log_{10}\left(\frac{\mathrm{max}}{\mathrm{clutter}}\right) \qquad (1)$$

where *max* and *clutter* are the maximum brightness of each absorber, and the average brightness of the clutter around each absorber, respectively. The brightness is calculated from the envelope of the beamformed after normalization and before log compression. Next, the absolute difference between the FWHM of the conventional and the refraction-corrected techniques divided by the FWHM of the conventional technique to show the percentage of improvement.

The power of the artifacts caused by the mode-converted shear waves and multiple scattering was reported with respect to the power of each absorber.

III. RESULTS AND DISCUSSION

A. *Numerical results*

Table I shows that the refraction-corrected technique improves both the ACR and resolution of TPA images.

TABLE I. The full-width-half-maximum and absorber-to-clutter ratio of the photoacoustic (PA) sources in the reference image and for the conventional and refraction-corrected method. The index of PA sources referred in Fig. 1. Ref, Conv, and Ref. Cor are the abbreviations for Reference, Conventional, and Refraction-Corrected, respectively.

PA source index	**Full-width-half-maximum (mm)**		**Absorber-to-clutter ratio (dB)**	
	Ref.	**Conv. / Ref. Cor.**	**Ref.**	**Conv. / Ref. Cor.**
1	0.29	0.96 / 0.55	34.9	22.3 / 26.7
2	0.28	0.55 / 0.4	36.4	24.7 / 28.2
3	0.28	0.75 / 0.47	36.1	22.4 / 24.2

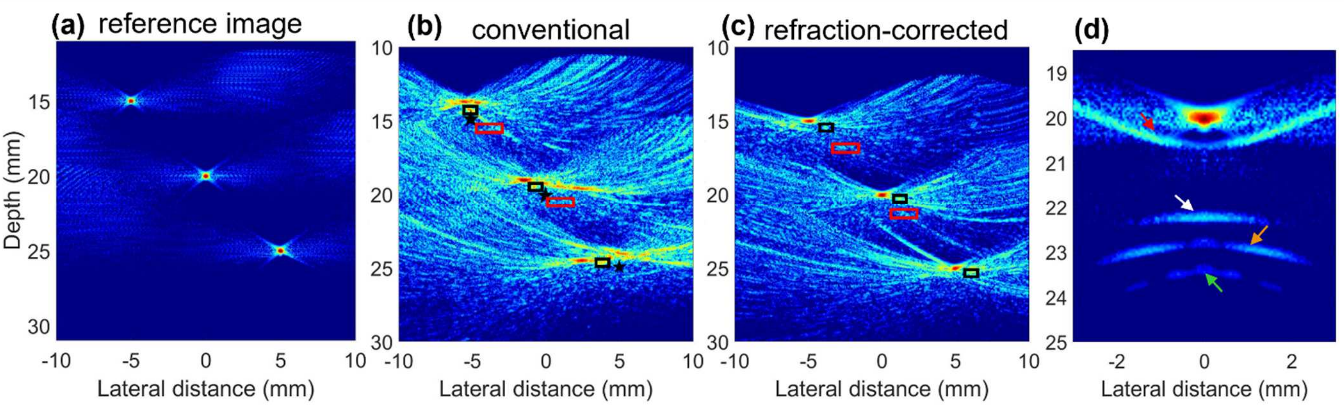

Fig. 2. The reconstructed image without (a) and images with the temporal layer in front of the probe (b-e). The reconstructed images using the conventional method (a, b) and the refraction-corrected method (c, d). The black star shows the true location of the photoacoustic sources, and the black, and red boxes show the mode-converted shear wave, all-compressional multiple scatterings. (d) The reconstructed image with the flat bone in front of the probe. Red, white, orange, and green arrows demonstrate the mode-converted shear wave, all-compressional, compressional-compressional-shear, and compressional-shear-shear multiple scatterings.

The average improvement of FHWH and ACR are 37% and 3.2 dB in comparison to the conventional reconstruction. This is because the bone layer was accurately described during image formation.

Fig. 2 (b) demonstrates the image reconstructed by the conventional method at the presence of a realistic bone model in front of the probe. All the skull-induced effects including refraction (the extension of the point spread function (PSF) in the lateral direction and the clutters around it), multiple scattering (red boxes), and mode-converted shear waves (black boxes) can be seen. In Fig. 2 (c) the extension of PSF caused by the refraction caused by the bone layer was corrected by the refraction-corrected technique.

Fig. 2 (d) shows the reconstructed image with the refraction-corrected method at the presence of a flat bone in front of the probe. Three types of multiple scattering (indicated by the white, orange, and green arrows) and the mode-converted shear wave (see the red arrow) are detectable.

Because the PSF was placed in lateral location of 0 mm, the incident angle of PA wave to the middle element of the transducer array is almost normal. This allowed us to calculate the travel times of the compressional and shear waves and the multiple scatterings. The first (the white arrow) second (the orange arrow) and third (the green arrow) multiple scatterings are caused by the all-compressional, compressional-compressional-shear, compressional-shear-shear wave reverberation in the bone layer, respectively. We identified the locations of multiple scattering (red boxes in Fig. 2) in a non-elastic simulation in which only the first type of multiple scattering (all-compressional) is generated.

We calculated the maximum power of red boxes in Fig. 2 and reported in Table II. It was not possible to identify the multiple scattering power of the third PA source as its effects were combined with the clutter around it. Table II shows that the power of multiple scattering decreased using refraction-corrected technique. This happens due to the accurate description of the bone layer and proper back-projection of the detected waves to the pixels which increases the power of the mainlobe.

To quantify the power of mode-converted shear waves, the image of non-elastic mode was subtracted from the elastic mode to identify their locations (black boxes), and then the maximum of each box calculated and reported in TABLE II. It can be seen that the power of mode-converted shear wave by refraction-corrected approach decreased.

TABLE II. The normalized power of mode-converted shear waves and all-compressional multiple scattering of the three PA sources for the conventional and refraction-corrected method. The index of PA sources referred in Fig. 1. Conv, and Ref. Cor are the abbreviations for Conventional, and Refraction-Corrected, respectively.

PA source index	**Power of mode-converted shear wave (dB)**	**Power of multiple scattering (dB)**
	Conv. / Ref. Cor.	**Conv. / Ref. Cor.**
1	-8.2 / -13.5	-16.9 / -18.4
2	-8.7 / -13.9	-20.7 / -21.8
3	-6.9 / -13.9	-

B. *Discussion, limitations and further work*

We have shown that the power of the mode-converted shear waves and multiple scattering differs in the images reconstructed by our refraction-corrected method and conventional image formation method. Of note, our reconstruction technique does not directly suppress the artifacts caused by the mode-converted shear waves and multiple scattering. It increases the power of the mainlobe (due to using the accurate travel times). Without normalizing the results to the maximum of each absorber, the power of the mode-converted shear waves and multiple scattering increases compared to when a conventional reconstruction is used, but also the power of the mainlobe (the maximum of each PSF). The increment of the power of the mainlobe is relatively significant though.

In our numerical model, the absorption coefficient for the both compressional and shear waves was set as the same and more importantly frequency-independent. However, the absorption of shear wave is almost twice that of compressional wave and both of them change according to the frequency [22]. This assumption was due to the limitations of the SimSonic in the modeling of absorption coefficient.

We considered the temporal bone as an isotropic layer while in practice it is anisotropic. Moreover, the temporal was defined as a single cortical bone, but in practice depending on the patient and also the location that the probe is placed on the skull, the bone might consist of three layers (cortical-cancellous-cortical) [9,25].

IV. CONCLUSION

In this work, we numerically evaluated the effects of mode-converted shear waves and multiple scattering through a realistic bone when the refraction caused by the bone layer was corrected. In average for all the absorbers, the refraction-corrected technique improves the ACR and FWHM by 3.2 dB and 37 %, respectively. With our technique, the average power of the mode-converted shear waves and all-compressional multiple scattering was 5.8 dB and 1.3 dB lower than that with the conventional image reconstruction technique, respectively. These improvements were due to the accurate description of the bone layer and proper back-projection of the waves to the pixels of the image, not directly suppressing the mode-converted shear wave and multiple scattering artifacts.

REFERENCES

[1] M. Xu and L. V. Wang, "Photoacoustic imaging in biomedicine," *Review of Scientific Instruments*, vol. 77, no. 4. 2006, doi: 10.1063/1.2195024.

[2] J. Yao and L. V. Wang, "Photoacoustic tomography: Fundamentals, advances and prospects," *Contrast Media Mol. Imaging*, vol. 6, no. 5, pp. 332–345, 2011, doi: 10.1002/cmmi.443.

[3] R. C. K. Jeeun Kanga, Xiuyun Liuc, Suyi Caoc, Steven R. Zeilerd, Ernest M. Grahame, Emad M. Boctora, "Transcranial photoacoustic characterization of neurovascular physiology during early-stage photothrombotic stroke in neonatal piglets in vivo," *J. Neural Eng.*, vol. 18, no. 6, p. 065001, 2022.

[4] X. J. Kang *et al.*, "Validation of noninvasive photoacoustic measurements of sagittal sinus oxyhemoglobin saturation in hypoxic neonatal piglets," *Appl Physiol*, pp. 983–989, 2018, doi: 10.1152/japplphysiol.00184.2018.

[5] J. A. Chalela *et al.*, "Magnetic resonance imaging and computed tomography in emergency assessment of patients with suspected acute stroke: a prospective comparison," *Lancet*, vol. 369, no. 9558, pp. 293–298, 2007, doi: 10.1016/S0140-6736(07)60151-2.

[6] M. E. Raichle, "Behind the scenes of functional brain imaging: A historical and physiological perspective," *Proc. Natl. Acad. Sci. U. S. A.*, vol. 95, no. 3, pp. 765–772, 1998, doi: 10.1073/pnas.95.3.765.

[7] J. Pfeuffer *et al.*, "Zoomed functional imaging in the human brain at 7 tesla with simultaneous high spatial and high temporal resolution," *Neuroimage*, vol. 17, no. 1, pp. 272–286, 2002, doi: 10.1006/nimg.2002.1103.

[8] X. Wang, D. L. Chamberland, and G. Xi, "Noninvasive reflection mode photoacoustic imaging through infant skull toward imaging of neonatal brains," *J. Neurosci. Methods*, vol. 168, no. 2, pp. 412–421, 2008, doi: 10.1016/j.jneumeth.2007.11.007.

[9] F. J. Fry and J. E. Barger, "Acoustical properties of the human skull," *J. Acoust. Soc. Am.*, vol. 63, no. 5, pp. 1576–1590, 1978, doi: 10.1121/1.381852.

[10] B. Liang *et al.*, "Impacts of the murine skull on high-frequency transcranial photoacoustic brain imaging," *J. Biophotonics*, vol. 12, no. 7, pp. 21–24, 2019, doi: 10.1002/jbio.201800466.

[11] B. Liang, S. Wang, F. Shen, Q. H. Liu, Y. Gong, and J. Yao, "Acoustic impact of the human skull on transcranial photoacoustic imaging," *Biomed. Opt. Express*, vol. 12, no. 3, p. 1512, 2021, doi: 10.1364/boe.420084.

[12] J. Shepherd, G. Renaud, P. Clouzet, and K. Van Wijk, "Photoacoustic imaging through a cortical bone replica with anisotropic elasticity," *Appl. Phys. Lett.*, vol. 116, no. 24, 2020, doi: 10.1063/5.0011260.

[13] G. Renaud, P. Kruizinga, D. Cassereau, and P. Laugier, "In vivo ultrasound imaging of the bone cortex," *Phys. Med. Biol.*, vol. 63, no. 12, p. aac784, 2018, doi: 10.1088/1361-6560/aac784.

[14] M. Mozaffarzadeh, C. Minonzio, N. De Jong, M. D. Verweij, S. Hemm, and V. Daeichin, "Lamb Waves and Adaptive Beamforming for Aberration Correction in Medical Ultrasound Imaging," *IEEE Trans. Ultrason. Ferroelectr. Freq. Control*, vol. 68, no. 1, pp. 84–91, 2021, doi: 10.1109/TUFFC.2020.3007345.

[15] M. Mozaffarzadeh, M. D. Verweij, V. Daeichin, N. De Jong, and G. Renaud, "Transcranial Ultrasound Imaging with Estimating the Geometry, Position and Wave-Speed of Temporal Bone," pp. 1–4, 2021, doi: 10.1109/ius52206.2021.9593826.

[16] M. Mozaffarzadeh, E. Verschuur, M. D. Verweij, N. De Jong, and G. Renaud, "Accelerated 2D Real-Time Refraction-Corrected Transcranial Ultrasound Imaging," *IEEE Trans. Ultrason. Ferroelectr. Freq. Control*, 2022, doi: 10.1109/TUFFC.2022.3189600.

[17] M. Mozaffarzadeh, E. Verschuur, M. D. Verweij, V. Daeichin, N. De Jong, and G. Renaud, "Refraction-Corrected Transcranial Ultrasound Imaging through the Human Temporal Window using a Single Probe," *IEEE Trans. Ultrason. Ferroelectr. Freq. Control*, no. February, 2022, doi: 10.1109/TUFFC.2022.3148121.

[18] C. Jiang *et al.*, "Ray Theory-Based Transcranial Phase Correction for Intracranial Imaging: A Phantom Study," *IEEE Access*, vol. 7, pp. 163013–163021, 2019, doi: 10.1109/ACCESS.2019.2951152.

[19] E. Bossy, M. Talmant, and P. Laugier, "Effect of bone cortical thickness on velocity measurements using ultrasonic axial transmission: A 2D simulation study," *J. Acoust. Soc. Am.*, vol. 112, no. 1, pp. 297–307, 2002, doi: 10.1121/1.1480836.

[20] B. Jing and, B. D. Lindsey, "Effect of skull porous trabecular structure on transcranial ultrasound imaging in the presence of elastic wave mode conversion at varying incidence angle," *Ultrasound Med. Biol.*, vol. 47, no. 9, pp. 2734–48, 2021.

[21] S. D. Sharma, E. Park, P. L. Purcell, K. A. Gordon, B. C. Papsin, and S. L. Cushing, "Age-related variability in pediatric scalp thickness: Implications for auditory prostheses," *Int. J. Pediatr. Otorhinolaryngol.*, vol. 130, no. November 2019, p. 109853, 2020, doi: 10.1016/j.ijporl.2019.109853.

[22] G. Pinton, J. F. Aubry, E. Bossy, M. Muller, M. Pernot, and M. Tanter, "Attenuation, scattering, and absorption of ultrasound in the skull bone," *Med. Phys.*, vol. 39, no. 1, pp. 299–307, 2012, doi: 10.1118/1.3668316.

[23] A. Y. Ammi *et al.*, "Characterization of Ultrasound Propagation Through Ex-vivo Human Temporal Bone," *Ultrasound Med. Biol.*, vol. 34, no. 10, pp. 1578–1589, 2008, doi: 10.1016/j.ultrasmedbio.2008.02.012.

[24] J. Peterson and P. C. Dechow, "Material properties of the human cranial vault and zygoma," *Anat. Rec. - Part A Discov. Mol. Cell. Evol. Biol.*, vol. 274, no. 1, pp. 785–797, 2003, doi: 10.1002/ar.a.10096.